DRAFT VERSION APRIL 8, 2025
Typeset using LaTeX **twocolumn** style in AASTeX631

Optimal Follow-Up of Gravitational-Wave Events with the UltraViolet EXplorer (UVEX)

LEO P. SINGER,[1,2] ALEXANDER W. CRISWELL,[3,4,5,6] SYDNEY C. LEGGIO,[3,4] R. WEIZMANN KIENDREBEOGO,[7,8,4] MICHAEL W. COUGHLIN,[3,4] HANNAH P. EARNSHAW,[9] SUVI GEZARI,[10,11] BRIAN W. GREFENSTETTE,[9] FIONA A. HARRISON,[9] MANSI M. KASLIWAL,[9] BRETT M. MORRIS,[11] ERIK TOLLERUD,[11] AND S. BRADLEY CENKO[1,2]

[1]*Astroparticle Physics Laboratory, NASA Goddard Space Flight Center, Greenbelt, MD 20771, USA*
[2]*Joint Space-Science Institute, University of Maryland, College Park, MD 20742, USA*
[3]*Minnesota Institute for Astrophysics, University of Minnesota, Minneapolis, MN 55455, USA*
[4]*School of Physics and Astronomy, University of Minnesota, Minneapolis, MN 55455, USA*
[5]*Department of Physics and Astronomy, Vanderbilt University, Nashville, TN 37240, USA*
[6]*Department of Life and Physical Sciences, Fisk University, Nashville, TN 37208, USA*
[7]*Laboratoire de Physique et de Chimie de l'Environnement, Université Joseph KI-ZERBO, Ouagadougou, Burkina Faso*
[8]*Artemis, Observatoire de la Côte d'Azur, Université Côte d'Azur, Boulevard de l'Observatoire, F-06304 Nice, France*
[9]*Division of Physics, Mathematics, and Astronomy, California Institute of Technology, Pasadena, CA 91125, USA*
[10]*Department of Physics and Astronomy, Johns Hopkins University, 3400 N. Charles Street, Baltimore, MD 21218, USA*
[11]*Space Telescope Science Institute, 3700 San Martin Drive, Baltimore, MD 21218, USA*

Submitted to PASP

ABSTRACT

The UltraViolet EXplorer (UVEX) is a wide-field ultraviolet space telescope selected as a NASA Medium-Class Explorer (MIDEX) mission for launch in 2030. UVEX will undertake deep, cadenced surveys of the entire sky to probe low mass galaxies and explore the ultraviolet (UV) time-domain sky, and it will carry the first rapidly deployable UV spectroscopic capability for a broad range of science applications. One of UVEX's prime objectives is to follow up gravitational wave (GW) binary neutron star mergers as targets of opportunity (ToOs), rapidly scanning across their localization regions to search for their kilonova (KN) counterparts. Early-time multiband ultraviolet light curves of KNe are key to explaining the interplay between jet and ejecta in binary neutron star mergers. Owing to high Galactic extinction in the ultraviolet and the variation of GW distance estimates over the sky, the sensitivity to kilonovae can vary significantly across the GW localization and even across the footprint of a single image given UVEX's large field of view. Good ToO observing strategies to trade off between area and depth are neither simple nor obvious. We present an optimal strategy for GW follow-up with UVEX in which exposure time is adjusted dynamically for each field individually to maximize the overall probability of detection. We model the scheduling problem using the expressive and powerful mathematical framework of mixed integer linear programming (MILP), and employ a state-of-the-art MILP solver to automatically generate observing plan timelines that achieve high probabilities of kilonova detection. We have implemented this strategy in an open-source astronomical scheduling software package called the Multi-Mission Multi-Messenger Observation Planning Toolkit (M^{4}OPT), on GitHub at https://github.com/m4opt/m4opt.

Keywords: Computational methods (1965) — Gravitational wave astronomy (675) — Open source software (1866) — Ultraviolet observatories (1739) — Ultraviolet transient sources (1854) — Wide-field telescopes (1800)

1. INTRODUCTION

In 2017, the Laser Interferometer Gravitational-Wave Observatory (LIGO) and Virgo (Abbott et al. 2017a) detected a long-duration gravitational wave (GW) inspiral signal, GW170817, at the same time that Fermi (Goldstein et al. 2017) and INTEGRAL (Savchenko et al. 2017) recorded a short gamma-ray burst (GRB), GRB 170817A. The alert sprang traps that had been set by hundreds of telescopes worldwide (Aasi et al. 2014; Abbott et al. 2016) which

leo.p.singer@nasa.gov

quickly found the optical counterpart (Coulter et al. 2017), AT2017gfo. As a measure of the degree to which the event focused the efforts of astronomers everywhere, the author list of Abbott et al. (2017b) runs to 24 pages!

The scientific harvest from this one event was remarkable. It fulfilled a three-decade-old dream of using GWs as "standard sirens" to measure the Hubble constant (Schutz 1986; Abbott et al. 2017c). Moreover, it proved once and for all the hypotheses that neutron star (NS) mergers are the central engines of short GRBs (Fong & Berger 2013; Abbott et al. 2017d) and the main cosmic factories of heavy r-process elements (Freiburghaus et al. 1999; Kilpatrick et al. 2017; Drout et al. 2017; Kasen et al. 2017).

It had long been understood that such mergers would tidally disrupt their NSs, and that radioactive decay of the heavy elements synthesized in their hot neutron-rich ejecta would fuel transients (Lattimer & Schramm 1974; Eichler et al. 1989; Li & Paczyński 1998) that came to be called kilonovae (KNe).

In those early days, astronomers assumed that the ejecta would have opacities similar to those in supernovae (SNe) and predicted fairly bright KN light curves that peaked in the optical or ultraviolet (UV) and that would be fairly easy to detect. However, further study of the atomic structure of lanthanides led to the realization that their dense absorption spectra would lead to line-blanketing in the optical, containing the radiation and only letting it leak out much more slowly and at longer wavelengths, in the infrared (Kasen et al. 2013). Observers grimly realized that although KNe were still among the most promising counterparts of NS mergers (Metzger & Berger 2012), they would be much dimmer, redder, and harder to detect than previously expected. Just how dim and red might depend sensitively on the masses and spins of the compact objects and whether either of them is a black hole (for a review, see Metzger 2020).

Although these later and more sober predictions agreed remarkably well with the observed spectral sequence of AT2017gfo at times later than a few days (Pian et al. 2017; Kasen et al. 2017; Villar et al. 2017; Kilpatrick et al. 2017; Drout et al. 2017), contrary to those expectations it was quite blue and featureless at the earliest observed times, less than a day after the merger (Shappee et al. 2017).

In the fallout from GW170817, the cause of this early optical and UV emission remains one of the most enduring mysteries. The blue emission could be radioactively powered but result from a geometrically distinct outflow component with higher velocity and/or lower lanthanide fraction (Nicholl et al. 2017) or could result from the shock caused by the "cocoon" interaction between the ejecta and the nascent jet (Kasliwal et al. 2017; Gottlieb et al. 2018; Piro & Kollmeier 2018). Lacking for GW170817, early-time UV observations, less than 12 hours after merger, could handily settle the debate (Arcavi 2018).

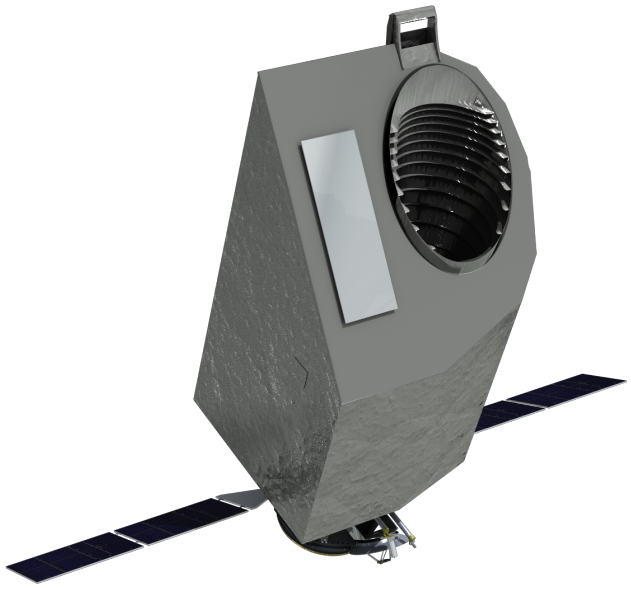

Figure 1. A rendering of UVEX. Reproduced from the concept study report (CSR).

1.1. *The Coming UV Time Domain Revolution*

More generally, there is a recognized gap in transient discovery capability in the UV, and an acknowledged need for a space-based UV wide-field time-domain survey (Sagiv et al. 2014). To meet this need, some of the authors proposed Dorado (née GUCI, Cenko 2019; Dorsman et al. 2023) to NASA as a Mission of Opportunity (MoO).

Although NASA made no MoO selection in that cycle, shortly thereafter the National Academies of Sciences, Engineering, and Medicine (2021) recommended in the 2020 decadal survey that "NASA should establish a time-domain program to realize and sustain the necessary suite of space-based electromagnetic capabilities required to study transient and time-variable phenomena, and to follow up multi-messenger events." NASA soon selected a much larger and more capable mission called the UltraViolet EXplorer (UVEX; Kulkarni et al. 2021; see rendering in Fig. 1)[1] as the next Medium-Class Explorer (MIDEX).

UVEX will have a wide, $3.5^\circ \times 3.5^\circ$ field of view (FOV) camera that will take images simultaneously in both a near ultraviolet (NUV; 1390–1900 Å) and a far ultraviolet (FUV; 2030–2700 Å) band reaching typical depths of $>$24.5 mag in a typical 900 s dwell. The imaging point spread function (PSF) diameter of about $\sim 2''$ will be well-matched to ground-based follow-up. It will also have a long-slit spectro-

[1] https://www.uvex.caltech.edu

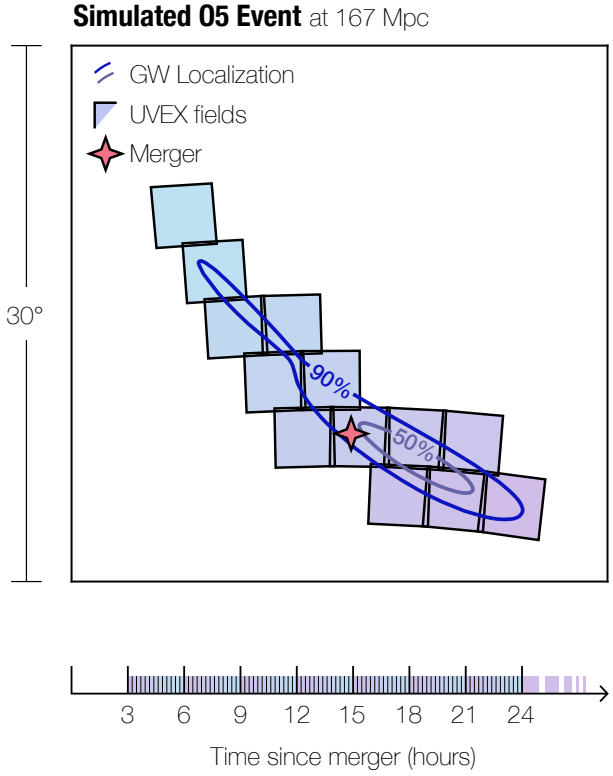

Figure 2. An example of a ToO observation sequence with UVEX to follow up a GW event. Adapted from Fig. D-8 from the UVEX CSR submitted to NASA HQ. This image was also reproduced as Fig. 14 in Kulkarni et al. (2021).

graph. UVEX will perform a mix of surveys with different sky coverage and cadence, and will observe the entire sky to at least >25.8 mag over the duration of the prime mission. UVEX will not just perform a transformative all-sky time-domain UV survey. It will also be able to perform targets of opportunity (ToOs) to follow up GW mergers and other multimessenger phenomena (see Fig. 2). With its wide FOV and two UV bandpasses, it should begin to probe the physical mechanism of early-time emission in KNe.

Meanwhile, other space agencies are working on complementary ultraviolet facilities. For example, Israel has a mission called the Ultraviolet Transient Astronomy Satellite (ULTRASAT; Shvartzvald et al. 2024) for which NASA has agreed to provide the launch. ULTRASAT will have an even larger FOV ($14^\circ \times 14^\circ$) than UVEX and will be ready for flight a few years before, but with some tradeoffs: it is much less sensitive (22.5 mag in 900 s), has a much larger PSF ($8\farcs3$ diameter), only a single imaging band (2300–2900 Å), and no spectrograph. Still, UVEX and ULTRASAT together will make a potent discovery engine for UV transients in general and GW counterparts in particular.

1.2. *A Multi-Mission Multi-Messenger Observation Planning Toolkit*

NASA selects Explorer-class missions on the basis of a concept study report (CSR) which undergoes several reviews, culminating in an in-person site visit (SV). In Criswell et al. (2025), we elaborated upon the case for GW follow-up with UVEX as we presented it to NASA in the CSR. That UVEX study leveraged the same GW ToO analysis and strategy that we had developed for the Dorado CSR. We envisioned our observation planning software, `dorado-scheduling`[2], as an early draft of what would eventually evolve into the observatory's real-time science operations software and a part of its public guest observer toolkit. Therefore, both studies benefited from an unusually high level of fidelity and realism for so early in their respective mission lifecycles.

The `dorado-scheduling` package considers, for any given ToO, the time-varying field of regard (FOR) constraints of the spacecraft, the spacecraft's slew time between any two target fields, the footprint on the sky of the instrument's FOV, and the probability distribution of the true but unknown position of the source — the GW localization map. Its purpose is to find the sequence of observations that maximizes the probability of detecting the counterpart. This can be surprisingly challenging: as with similar "hard" optimization problems (e.g. the "traveling salesman" problem), the combinatorial scale makes a brute-force search of all possible observation sequences out of the question. On the other hand, simple strategies can yield unacceptable results. For example, observing the fields in descending order of probability may be a poor strategy if it causes one to miss fields that pass out of the FOR early on, or if it results in long slew times. Moreover, it may be labor-intensive to adjust or rewrite any handmade strategy to re-tune it for changes to the mission design. Instead of such sub-optimal heurstics, `dorado-scheduling` directly and globally optimizes the predicted probability of detection using the versatile and expressive mathematical framework of mixed integer linear programming (MILP; see textbooks of Chen et al. 2009a and Williams 2013a), and employs IBM's state-of-the-art MILP solver, CPLEX,[3] to search for the global optimum.

Responding to queries during the Dorado SV about varying extinction and foregrounds, we added a powerful capability to dynamically optimize the exposure time of each field to adjust for spatial variations in sensitivity. This refinement brought in several new possible tradeoffs to increase detection probability. For example, the GW localization is a distribution over both sky location and distance, and there is a Malmquist-like tendency for regions of high probability on

[2] https://github.com/nasa/dorado-scheduling

[3] https://www.ibm.com/products/ilog-cplex-optimization-studio

the sky to favor large distances (Singer et al. 2016a), so at times it is advantageous to observe lower probability fields that require less exposure time. Furthermore, UV sensitivity varies significantly across the sky. For instance, it may be beneficial to spend less time observing high-probability fields that also have high Milky Way dust extinction. The MILP framework allowed us to take advantage of these additional degrees of freedom without needing to meticuluously craft the observing strategy itself.

In our simulations, adaptive exposure time greatly improved the detection efficiency of the mission. In earlier related works, Coughlin & Stubbs (2016) derived power-law expressions for optimal exposure time under simplified conditions. Chan et al. (2017) varied exposure times but without considering field-to-field variation in distance, variation in sensitivity, or FOR constraints. Herner et al. (2020) employed exposure time maps to select feasible fields for ToO observations. Liu et al. (2021) varied exposure time in accordance with the expected time-dependence of the light curve. However, we believe that our *adaptive optimization of exposure time for each field, accounting for spatial variation in distance estimate and sensitivity, to globally maximize the probability of detection, is novel*. Unfortunately, this code was not used in the UVEX study or in Criswell et al. (2025).

The `dorado-scheduling` code also had the major limitation that it was released under the obscure and anachronistic NASA Open Source Agreement (NOSA), which placed severe obstacles to our own collaborators using or contributing to it. The lawyers at Goddard Space Flight Center (GSFC) continue to require all GSFC scientists to employ NOSA even though it has has been rejected by the Free Software Foundation (2006), the National Academies of Sciences, Engineering, and Medicine (2018), and even the NASA Science Mission Directorate (2022). Fortunately, NASA HQ intervened in this case and we were permitted to establish a new, truly open-source, permissively licensed software project, which anyone can contribute to and use. However, this required a rewrite which took several years.

In this paper, we finally present the Multi-Mission Multi-Messenger Observation Planning Toolkit (M^4OPT), which has many other advances over earlier work:

- It is released under a permissive, mainstream license (the Berkeley Software Distribution, or BSD, license) to promote adoption and contribution by the community.
- It is designed from the start to support multiple missions, including UVEX and ULTRASAT. We envision supporting both space- and ground-based observatories in the future.
- It can adjust exposure times given the anticipated absolute magnitude and the three-dimensional GW localization distribution in sky position and distance.
- It can dynamically vary the exposure time of each field to pierce through spatial variations in foregrounds (zodiacal light, Galactic diffuse emission) and dust extinction.
- It can be given the anticipated absolute magnitude of the source as either a point estimate or a distribution with Gaussian uncertainty.
- The dynamic exposure times are made possible by a `numpy` (Harris et al. 2020) vectorized exposure time calculator (ETC) which enables large parameter sweeps of synthetic photometry calculations which are otherwise prohibitively slow with synphot (STScI Development Team 2018) alone.
- It models additional spacecraft dynamics effects, including the roll angle of the telescope which is determined by solar power requirements.
- It already complies fully with NASA Procedural Requirements (NPR) 7150 (NASA 2022) software engineering practices for "Class C" software, and has 95% test coverage.
- It is deeply integrated with the Astropy (Astropy Collaboration et al. 2013, 2018) ecosystem, and has an interface that is based on Astropy coordinates, units, and model classes.

In this paper, we describe the mathematical approach of M^4OPT, and then use it to produce realistic ToO observing sequences with UVEX for simulated GW events. An example M^4OPT observing plan is shown in Fig. 3 and Table 1. We show that the new dynamic exposure time capabilities dramatically increases the probability of KN detection.

2. MILP PROBLEM FORMULATION

Linear programming (LP) is a mathematical optimization formalism in which one represents an objective as a linear combination of decision variables, subject to constraints that take the form of a system of linear inequalities. The canonical form a LP is

$$\begin{aligned} \text{Find} \quad & \mathbf{x} \in \mathbb{R}^N \\ \text{that maximizes} \quad & \mathbf{c}^\mathsf{T}\mathbf{x} \\ \text{subject to} \quad & \mathbf{A}\mathbf{x} \leq 0 \\ \text{and} \quad & \mathbf{x} \geq 0. \end{aligned}$$

Table 1. An example M[4]OPT observing plan (same as Fig. 3).

			Location[c]			Target[d]		Sky map						
Time[a]	Dur.[b]	Action	x	y	z	R.A.	Dec.	Roll	Prob.[e]	Dist.[f]	Lim.[g]	Dust[h]	Sky[i]	Det. Prob.[j]
10:23:42	325	observe	-183	142	-50	31.6571	-23.5560	-138	0.04	255	24.07	0.07	27.36	0.01
10:29:06	120	slew	—	—	—	—	—	—	—	—	—	—	—	—
10:31:06	767	observe	-179	148	-50	32.4155	-28.4429	-141	0.15	278	24.83	0.07	27.48	0.08
10:43:53	127	slew	—	—	—	—	—	—	—	—	—	—	—	—
10:46:00	1348	observe	-168	160	-50	36.9122	-33.0462	-146	0.21	320	25.29	0.11	27.54	0.11
11:08:28	107	slew	—	—	—	—	—	—	—	—	—	—	—	—
11:10:15	1529	observe	-149	179	-50	39.3087	-35.3375	-149	0.11	345	25.39	0.16	27.57	0.05
11:35:44	127	slew	—	—	—	—	—	—	—	—	—	—	—	—
11:37:51	3006	observe	-125	197	-50	34.6192	-30.7459	-143	0.27	296	25.84	0.10	27.51	0.19
12:27:57	120	slew	—	—	—	—	—	—	—	—	—	—	—	—
12:29:57	2166	observe	-75	223	-50	33.7574	-25.7998	-141	0.16	269	25.58	0.07	27.40	0.11
13:06:04	108	slew	—	—	—	—	—	—	—	—	—	—	—	—
13:07:51	924	observe	-34	234	-50	35.9256	-28.0474	-144	0.17	284	24.97	0.08	27.43	0.09
13:23:15	107	slew	—	—	—	—	—	—	—	—	—	—	—	—
13:25:02	767	observe	-15	236	-50	32.4155	-28.4429	-141	0.15	278	24.83	0.07	27.48	0.08
13:37:49	120	slew	—	—	—	—	—	—	—	—	—	—	—	—
13:39:49	325	observe	1	237	-50	31.6571	-23.5560	-138	0.04	255	24.07	0.07	27.36	0.01
13:45:14	108	slew	—	—	—	—	—	—	—	—	—	—	—	—
13:47:01	2166	observe	9	237	-50	33.7574	-25.7998	-141	0.16	269	25.58	0.07	27.40	0.11
14:23:08	108	slew	—	—	—	—	—	—	—	—	—	—	—	—
14:24:55	924	observe	51	233	-50	35.9256	-28.0474	-144	0.17	284	24.97	0.08	27.43	0.09
14:40:19	104	slew	—	—	—	—	—	—	—	—	—	—	—	—
14:42:04	3006	observe	70	229	-51	34.6192	-30.7459	-143	0.27	296	25.84	0.10	27.51	0.19
15:32:10	107	slew	—	—	—	—	—	—	—	—	—	—	—	—
15:33:57	1348	observe	123	207	-51	36.9122	-33.0462	-146	0.21	320	25.29	0.11	27.55	0.11
15:56:25	107	slew	—	—	—	—	—	—	—	—	—	—	—	—
15:58:12	1529	observe	146	192	-51	39.3087	-35.3375	-149	0.11	345	25.39	0.16	27.57	0.05

[a] UTC start time of scheduled action on the arbitrary date of 2012-06-01.

[b] Duration (s) of scheduled action.

[c] Cartesian coordinates (Mm) of the spacecraft in the Earth-fixed (International Terrestrial Reference System) frame.

[d] Target location (deg) in the equatorial (International Celestial Reference System) frame.

[e] Integral of the GW probability sky map over this field: probability that the true, but unknown, position of the source is within the footprint.

[f] *A posteriori* mean GW distance estimate (Mpc) over this field.

[g] Median limiting magnitude (AB mag) over this field.

[h] Median dust extinction in band (AB mag) over this field.

[i] Median sky surface brightness in band (AB mag arcsec^{-2}) over this field.

[j] Contribution by this field to the predicted probability of detection.

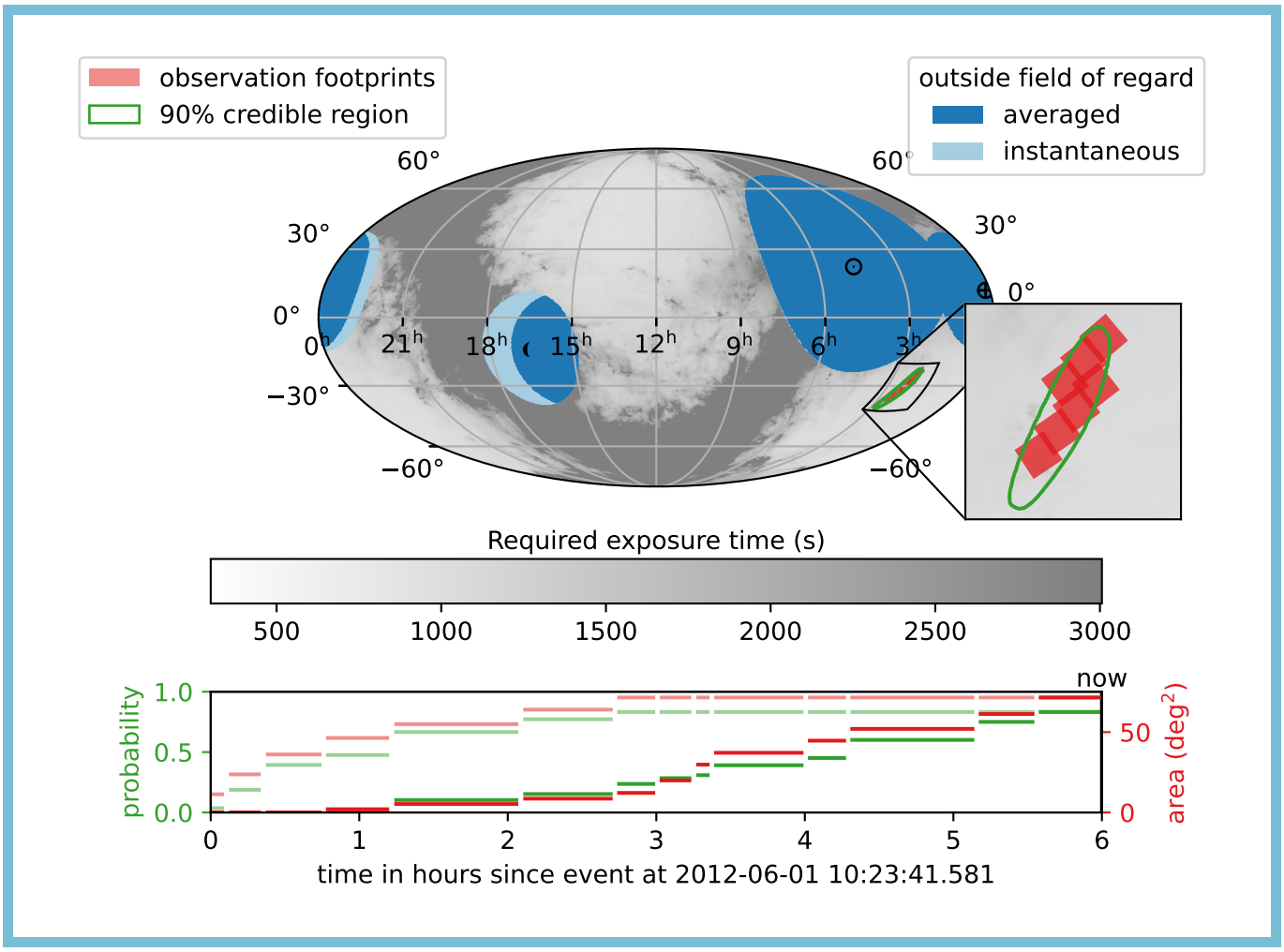

Figure 3. An example M[4]OPT observing plan. **Top panel** and **inset**: The footprints of the observations filled in pink, the 90% credible region of the GW localization outlined in green, the region that is always outside of the FOR (referred to in the legend as the "averaged" FOR) filled in deep blue, and the region that is outside of the instantaneous FOR filled in light blue. **Bottom panel**: The timeline of the accumulation of detection probability and area. The region that has been covered by one visit is shown in pale red and green, whereas the region that has been covered by two visits is shown in deep red and green. This figure is available as an animation.

LP is useful for problems of resource allocation. If instead of being reals, certain of the decision variables are required to be integers, then the problem is called mixed integer linear programming (MILP). MILP allows one to model situations where some decision variables represent alternative courses of action or where some constraints are Boolean in nature. The textbook chapters of Chen et al. (2009b) and Williams (2013b) serve as useful translation dictionaries from logical constraints to integer linear ineqalities.

There are a variety of free and open source MILP solvers; the most readily available for Python users is HiGHS (Huangfu & Hall 2018) which now can be called directly from SciPy (Virtanen et al. 2020). However, the best commercial MILP solvers are much faster and can handle much larger problems than any current open-source software (Koch et al. 2011; Huangfu & Hall 2018). Although M^{4}OPT itself is open source, it calls the commercial MILP solver CPLEX by IBM. CPLEX is free for academic and research use by students, faculty, and staff at academic institutions. For non-academic users, its pricing is comparable in cost to mid-range computer-aided design software.

Common applications of MILP include planning and scheduling. There are already many noteworthy and successful uses of MILP to astronomical observation planning. Las Cumbres Observatory (LCO) uses it to allocate observations on a global queue-scheduled network of telescopes (Saunders et al. 2014). Zwicky Transient Facility (ZTF) uses it to multiplex several sky surveys with different coverage and cadence requirements on a single telescope (Bellm et al. 2019), and our colleagues have proposed using it to schedule ToO observations with ZTF (Parazin et al. 2022). It has been applied to scheduling observing programs on Atacama Large Millimeter/Submillimeter Array (ALMA; Solar et al. 2016) and exoplanet searches on Keck (Handley et al. 2024).

2.1. *The Maximum Weighted Coverage Problem*

The classic maximum weighted coverage problem (MWC) has a MILP representation that is at the core of our ToO planning problem. In MWC, one has a finite sequence of real-valued weights, $(w_j)_j$, and a finite set of sets, $S = \{S_i\}_i$, over the integers, $\forall i : S_i \subset \mathbb{Z}$. The objective is to find a subset $S' \subseteq S$, with a maximum cardinality $|S'| \leq k$, that maximizes the sum over all of the weights $\sum_{j \in \bigcup S'} w_j$. This is illustrated in Fig. 4. The MWC has a straightforward MILP representation:

$$\begin{aligned} \text{Maximize} \quad & \sum_j y_j w_j \\ \text{subject to the constraints} \quad & \sum_i x_i \leq k \\ \text{and} \quad & \sum_{i|j \in S_i} x_i \geq y_j. \end{aligned}$$

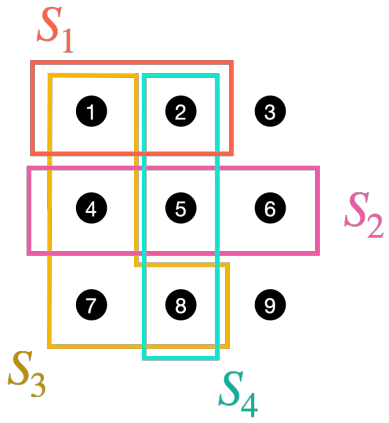

Figure 4. Illustration of MWC. Four sets $S = \{S_1, S_2, S_3, S_4\}$ are represented as regions with colored borders. The elements of those sets are represented by black numbered circles.

The most basic version of our ToO problem is that we want to maximize the total integrated probability that the true, but unknown, position of the source is within one or more of the footprints that we select to observe. Each GW alert comes with a localization sky map that gives the posterior probability distribution of the sky position as an image that is sampled on a Hierarchical Equal Area isoLatitude Pixelization (HEALPix; Górski et al. 2005) grid. The weights $(w_j)_j$ are the probability values and the subsets $(S_i)_i$ are the HEALPix pixels contained within the footprints of the FOV on a reference grid of allowed pointings of the telescope (see Fig. 5). The solution of the MWC problem gives us the optimal pointings of the telescope and the HEALPix pixels contained within all of the planned observations.

2.2. *Scheduling Constraints*

Scheduling problems in which there are time intervals that must be disjoint are also prominent in classic applications of MILP. Consider two intervals, both of duration δ, and each centered on the real-valued event times t_0 and t_1 respectively, and both intervals of duration δ. Suppose also that the event times t_0 and t_1 are both restricted to the range from 0 to M. If the two intervals must be disjoint, then we can express the situation with the following system of ineqalities:

$$\begin{aligned} 0 \leq t_0 \leq M \\ 0 \leq t_1 \leq M \\ |t_1 - t_0| \geq \delta. \end{aligned}$$

The last inequality is nonlinear because it contains the absolute value function. By introducing a binary decision variable a, we can transform it into two linear inequalities,

$$\begin{aligned} t_1 - t_0 - \delta \leq M(1 - a) \\ t_0 - t_1 - \delta \leq Ma. \end{aligned}$$

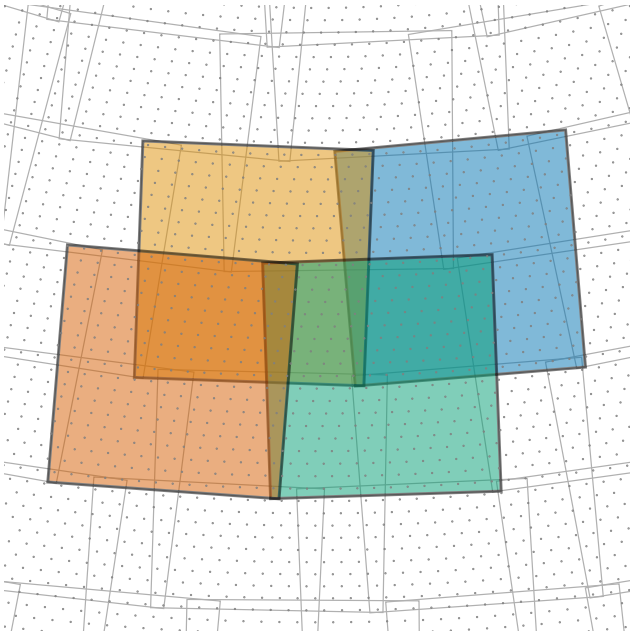

Figure 5. MWC applied to coverage of a region on the sky by multiple partially overlapping fields. The centers of HEALPix pixels are marked with gray dots.

In our ToO problem, the times t_0 and t_1 represent the times of observations of two different fields that must be executed by a single telescope, and the duration δ represents the exposure time plus slew time. By extending to more than two intervals we can model scheduling of a sequence of observations by one telescope.

2.3. *The Full Problem*

The full ToO problem as it is modeled and solved by M^{4}OPT has elements of the MWC and elements of scheduling. The reader may find the full MILP problem setup in Appendix A, in which we develop three successively more elaborate models, finally arriving at the full problem as it is implemented by M^{4}OPT. These three stages are:

Section A.1, Fixed Exposure Time—We may observe any fields within the instantaneous FOR. Each field must be visited twice with a minimum cadence between visits. Every field has the same fixed exposure time. The objective is to maximize the probability that the true (but unknown) position of the source is within any of the selected fields. The probability of detection is integrated over the two-dimensional GW localization map.

Section A.2, Variable Exposure Time—As in Section A.1, but each field's exposure time may vary. We assume that the apparent magnitude of the source is fixed with respect to time and known precisely, and the objective is to maximize the probability that the limiting magnitude at the true (but unknown) location of the source exceeds that apparent magnitude. The probability of detection is integrated over the two-dimensional GW localization map and employs a sky map of the limiting magnitude as a function of exposure time.

Section A.3, Variable Exposure Time with Prior Distribution of Absolute Magnitude—As in Section A.2, but we no longer know the apparent magnitude of the source. Instead we have a luminosity function, a probability distribution over its true (but unknown) absolute magnitude, which is fixed with respect to time. We also have a three-dimenisional GW localization map in right ascension, declination, and luminosity distance. The probability of detection is integrated over the 3D localization map and the luminosity function.

Table 2. ETC toy model parameters.

Quantity	Value
Aperture diameter	75 cm
Pixel scale	$1''$ pix^{-1}
PSF sharpness[a]	$1/(4\pi)$
Gain	0.85
Read noise	2 ct
Dark noise	10^{-3} ct s^{-1}
NUV response[b]	$0.2\sqrt{2\pi}\phi[(\lambda - 2300\ \text{Å})/(180\ \text{Å})]$
FUV response[b]	$0.15\sqrt{2\pi}\phi[(\lambda - 1600\ \text{Å})/(100\ \text{Å})]$

[a] We assume optimal PSF photometry with Nyquist pixel sampling, that is, a sharpness of $1/4\pi$ (Mighell 2005).

[b] The function $\phi(x)$ is the standard normal distribution.

3. EXPOSURE TIME ESTIMATION

The reference ETC for UVEX is still closed source because the instrument is still evolving in small details. We use M^{4}OPT's open-source toy model of the instrument performance that roughly reproduces the public sensitivity curve plot on the UVEX web site[4] (see Fig. 6). The parameters of the toy model are listed in Table 2.

We need to perform about 1 million ETC calculations at different sky positions and apparent magnitudes for each event. The `synphot` Python package (STScI Development Team 2018) is the standard tool for synthetic photometry. Unfortunately, it would be prohibitively time-consuming to set up and evaluate 1 million `synphot` scenarios due to the overhead of creating all of the Python objects involved. Our `m4opt.synphot` module accelerates synthetic photometry

[4] https://www.uvex.caltech.edu/page/for-astronomers; accessed 2025-01-26

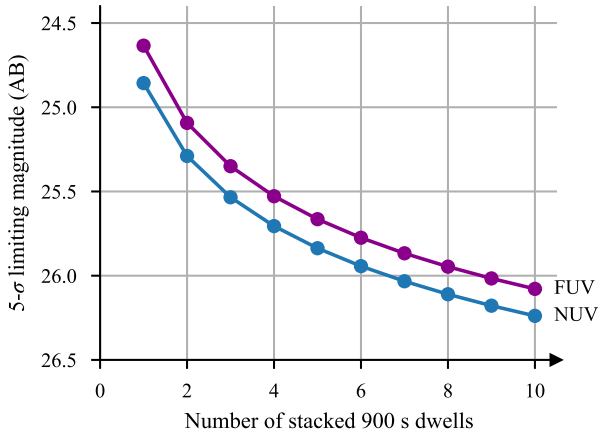

Figure 6. Median limiting magnitude, averaged over target coordinates and observation time.

calculations by using the symbolic algebra package `sympy` (Meurer et al. 2017) to rearrange the `synphot` model tree into additive components with separable spatial dependence that can be integrated separately and then added back together. For nonlinear components (i.e., extinction), we do a parameter sweep and employ interpolation. The result is many orders of magnitude faster than `synphot` and contributes only about a second of run time to the scheduler.

There are three spatially-dependent spectral components in the ETC:

Zodiacal light—We modeled zodiacal background light by taking the "high" sky background spectrum from the Hubble Space Telescope Imaging Spectrograph (STIS) Instrument Handbook (Rickman & Brown 2024) and scaling it by a spatially-dependent factor resulting from bilinear interpolation of the tables of Leinert et al. (1998). In the future, we plan to replace the spatial dependence with `zodipy` (San et al. 2022; San 2024), which has a higher spatial resolution and is valid for locations throughout the Solar System beyond Earth orbit.

Galactic diffuse background—Murthy (2014) provides piecewise cosecant fits to the surface brightness of Galactic diffuse emission in the two GALEX bands. We employ these fits to get the spatial dependence, and obtain the wavelength dependence by interpolating and extrapolating linearly through the two bands.

Dust extinction—To model extinction due to dust in the Milky Way, we use the Gordon et al. (2023) model (see also Gordon et al. 2009; Fitzpatrick et al. 2019; Gordon et al. 2021; Decleir et al. 2022) as implemented in the `dust_extinction` Python package (Gordon 2024). We employ a fixed total-to-selective extinction ratio $R(V) = 3.1$ and obtain $E(B-V)$ reddening values as a function of sky position using the Planck Collaboration et al. (2016) model as implemented by the `dustmaps` Python package (Green 2018).

4. CASE STUDY: GW OBSERVATIONS WITH UVEX

Here we explain the setup of M^{4}OPT for UVEX.

GW localizations—We started with the same simulated GW localizations as Criswell et al. (2025), which covers LIGO, Virgo, and KAGRA's fifth (O5) and sixth (O6) observing runs. The data are publicly archived in Kiendrebeogo (2025). These simulated events were generated using the same methodology as Petrov et al. (2022) and Kiendrebeogo et al. (2023), except that the signal to noise ratio (S/N) threshold for GW detection is set to 10. The localizations were generated with the rapid localization engine BAYESTAR (Singer & Price 2016) and consist of 3D posterior probability distributions of sky location and luminosity distance (Singer et al. 2016a,b). Like Criswell et al. (2025), we selected only those events for which the rest frame secondary (lighter) compact object mass m_2 was $\leq 3M_\odot$ to pick only events that could plausibly be binary neutron star (BNS) or neutron star–black hole (NS–BH) binaries.

KN absolute magnitude distribution—Kulkarni et al. (2021) considers two alternative KN scenarios: nucleosynthesis powered or shock powered. For the former, they employ the semi-analytic r-process heating model of Hotokezaka & Nakar (2020); for the latter, the analytical shock model of Piro & Kollmeier (2018). For both models, Appendix E.2 of Kulkarni et al. (2021) specifies fiducial parameter ranges and the 90% credible intervals for the peak absolute magnitude in each band. These absolute magnitude ranges are reproduced in the Table 3. UVEX observes in both the NUV and FUV filters simultaneously, and our objective is to detect the source in both bands. Therefore we should plan observations using the fainter of the two models and the fainter of the two bands: the nucleosynthesis-powered model in FUV, with an absolute magnitude range of $[-14.5, -10.2]$. Assuming that this is the 90% credible interval of a Gaussian distribution, the absolute magnitude has the approximate distribution

$$M_{\mathrm{NUV}} \sim \mathcal{N}(-12.4, 1.3). \quad (1)$$

Follow-up time window—Criswell et al. (2025) required a single epoch of UVEX observations to take 3 hours or less. To match this choice, we configure M^{4}OPT to plan two visits of each field with a minimum cadence of 30 min between repeated visits, with a total elapsed time limit of 6 hours.

Exposure time limits—The exposure time is allowed to vary adaptively for each field, with a minimum exposure time of $\epsilon_{\mathrm{min}} = 300$ s. The minimum exposure time corresponds to a single standard UVEX imaging exposure. (A standard survey dwell consists of 3 consecutive stacked 300 s exposures.)

Table 3. Ranges of peak absolute magnitudes of KNe. Adapted from Appendix E.2 of Kulkarni et al. (2021).

	Absolute magnitude range	
Model	NUV	FUV
Nucleosynthesis powered	[-15.6, -12.4]	[-14.5, -10.2]
Shock powered	[-17.8, -15.3]	[-17.9, -15.0]

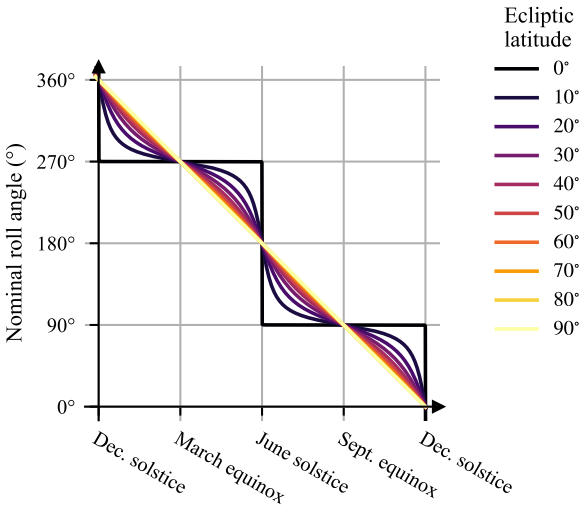

Figure 7. Nominal roll angle as a function of time for selected ecliptic latitudes.

FOV—Like most space telescopes, UVEX has solar panels that rotate on a solar array drive assembly perpendicular to the telescope boresight (see Fig. 1). The position angle of observations is fixed to the nominal roll angle that allows the spacecraft to orient the solar panels perpendicular to the Sun while keeping the cold side of the spacecraft facing away from the Sun. For any given target position, the roll angle goes through one revolution per year. For targets at the ecliptic poles, the nominal roll angle varies linearly with time. For targets in the ecliptic plane, the nominal roll angle flips by 180° at the solstices. At all intermediate ecliptic latitudes, the roll angle oscillates smoothly in a manner that interpolates between these extremes (see Fig. 7). Because the roll angle changes slowly on the timescale of a day, we calculate the nominal roll angle for each field at the time of the event, and leave it fixed at that value for the duration of the observing plan.

Slew time—To estimate the time to slew between any two fields, we employ a simplified model of the spacecraft dynamics in which the spacecraft has a maximum angular acceleration of $0.^{\circ}006\ \mathrm{s}^{-2}$ and maximum angular rate $0.^{\circ}6\ \mathrm{s}^{-1}$

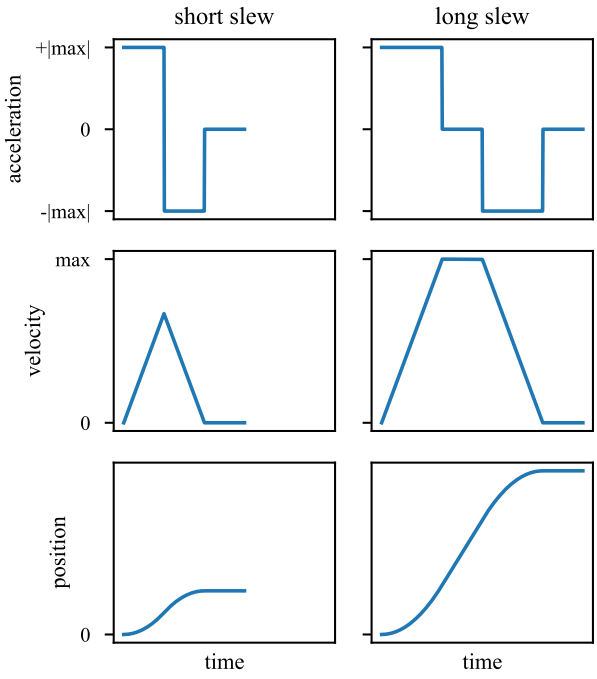

Figure 8. The slew model consists of an acceleration phase at the maximum acceleration, possibly a coasting phase at the maximum angular velocity, a deceleration phase at the maximum acceleration, and a settling phase.

about any axis, plus a fixed settling time of 60 s. We assume that the spacecraft executes an eigenaxis maneuver, rotating through the smallest possible angle about a single axis, following a "bang-bang" angular rate profile illustrated in Fig. 8. (Note that even for a symmetric moment of inertia, this eigenaxis maneuver is *not* the fastest possible slew; see Bilimoria & Wie 1993.) With this model, it takes 108 s to slew by the width of the FOV and 460 s to slew by 180°.

HEALPix resolution—We discretize the footprint of the FOV on a HEALPix grid with $n_{\mathrm{side}} = 128$, which is sufficient to resolve the square shape of the FOV (see Fig. 9.

Field grid—The centers of the fields are the vertices of a $\{3, 5+\}_{21,4}$ icosahedral geodesic polyhedron (see Fig. 10) generated using the `antiprism` software by Adrian Rossiter[5]. This grid ensures that all of the fields cover the sky without gaps, regardless of roll angle.

Run duration—As in Criswell et al. (2025), we assumed 1.5 years of overlap between the UVEX prime mission and the GW observing run.

[5] https://github.com/antiprism/antiprism

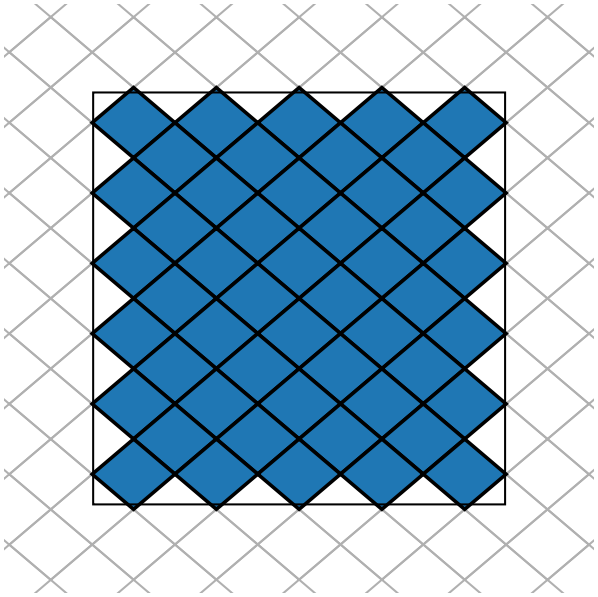

Figure 9. The footprint of the UVEX FOV discretized on a HEALPix grid with $n_{\rm side} = 128$. The footprint, or the region on the sky that is contained within the FOV in one observation, is shown as the solid gray square. The edges of HEALPix pixels are depicted as light gray lines. The HEALPix pixels whose centers are within the footprint are filled in blue.

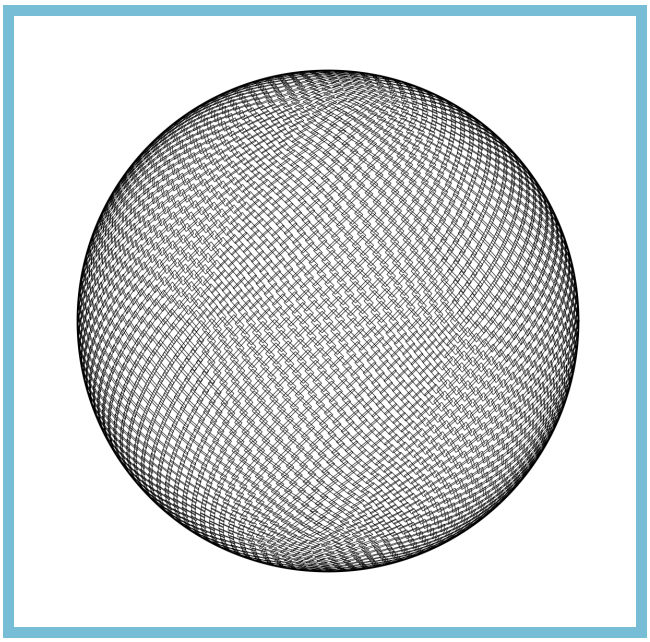

Figure 10. Footprints of the UVEX FOV on the geodesic reference grid. This figure is available as an animation that shows the variation in position angle of each field with time.

Follow-up selection criterion—We ran M^{4}OPT on all simulated events. We consider an event selected for follow-up if the scheduler's objective value P is less than $P^* = 0.1$. As the MILP solver runs, it keeps track of both the best objective value of any solution found so far—the "incumbent" solution—and an upper bound on the objective value of any solution, including as-yet unexplored solutions. Normally the solver would terminate when the gap between the incumbent objective value and the best bound close to within some numerical tolerance, but we also configure the solver to stop early if the best bound ever drops below P^* because the event in question will not be selected for follow-up.

Recall from Section A.3 that the scheduler's objective value is (a numerical approximation of) the probability of detection—integrated over the absolute magnitude, sky position, and distance, none of which are known to the scheduler. We stress that our strategy for selecting which events to trigger is to simply run the scheduler for every single event and proceed if the predicted detection probability is at least 10%.

This is conceptually very different from the selection criteria in Criswell et al. (2025) which is based on the 90% credible area, $A_{90\%}$, and luminosity distance $d_{\rm L}$ of the event. However, we can predict analytical thresholds on both of these quantities that will be roughly equivalent to our strategy:

$$d_{\rm L} < d_{\rm L}^* = 10^{\frac{1}{5}(x^* - \mu_X + \sigma_X \Phi^{-1}(1-P^*) - 25)}\ {\rm Mpc} \quad (2)$$

$$A_Q < A_Q^* = \left(\frac{\Psi^{-1}(Q)}{\Psi^{-1}(P^*)}\right)^2 \left(\frac{\delta - \beta}{\epsilon_{\rm min} n_K}\right) A_{\rm FOV} \quad (3)$$

$$\frac{A_Q}{A_{\rm FOV}} < \left(\frac{d_{\rm L}}{d_{\rm L}^*}\right)^{-4} \quad (4)$$

A_Q is the Qth percentile credible region, x^* is the faintest limiting magnitude at any point on the sky, $A_{\rm FOV}$ is the area of the FOV, $\Phi^{-1}(x)$ is the inverse of the cumulative distribution function (CDF) of the standard normal distribution, and $\Psi^{-1}(x) = -2\ln(1-x)$ is the inverse of the CDF of a χ^2 distribution with 2 degrees of freedom.

4.1. *Results*

All simulated events are listed in the online version of Table 4. Because these are simulated events, we can determine the probability of detection for each event given its true sky location and distance. To calculate the detection probability, we calculate the limiting absolute magnitude at that true position and distance for the longest exposure that contains that position (or an exposure time of zero if the true sky position is not contained in any planned observation). The detection probability is simply the CDF of the absolute magnitude distribution, Eq. (1), evaluated at that limiting absolute magnitude.

In Fig. 11, we show both the scheduler objective value and the detection probability on a scatter plot of the 90% credi-

ble area and the luminosity distance of events. As we would expect, both the objective value and detection probability increase as the area and distance of the events decrease.

In Table 5, we list the expected numbers of events selected for follow-up and the number of KNe detected over 1.5 years of observation. The number of events selected is simply the number of observing plans with objective value ≥ 0.1. The expected number of KNe detected is the sum of the detection probabilities of all of the events.

As in Petrov et al. (2022) and in Kiendrebeogo et al. (2023), this table gives central 90% credible intervals about the median, incorporating a lognormal uncertainty in the BNS merger rate of 210^{240}_{-120} Gpc^{-3} yr^{-1} and Poissonian variation in the number of events over a finite time duration.

If instead of optimizing for a detection in both filters, we optimize for a detection in *at least one filter*, then both the number of events selected and the number of events detected approximately double.

5. CONCLUSION

Unfortunately, direct comparisons of the rates in Table 5 to Criswell et al. (2025), which used `dorado-scheduling` and a fixed exposure time for each event, are not meaningful because we made many refinements to the starting assumptions. The following change would lead to a higher detection rate:

- We used a slightly brighter distribution of absolute magnitudes that is consistent with the stated KN model ranges in Kulkarni et al. (2021).

The following change would lead to a lower detection rate:

- We used a much denser and more heavily overlapping grid of fields in order to ensure complete coverage of the sky at all roll angles.

Our trigger and detection rates in Table 5 are comparable with the most optimistic estimates in Criswell et al. (2025). Although by itself this comparison is not informative on the merits of these two strategies, it is a positive result for the prospects of KN detection with UVEX.

More quantitatively, we can show that the dynamic exposure time strategy results in a higher detection probability than any given fixed exposure time for a given event. Fig. 12 shows a typical example. This is a plot of detection probability (without knowledge of the position of the source) versus exposure time for observing plans for a single event generated using the formulation from Section A.1. The detection probability for the dynamic exposure time strategy from Section A.3 is shown as a horizontal dashed line.

This novel dynamic exposure time observing strategy is promising for GW follow-up with any large FOV imaging instrument. Although we have focused on UVEX, we encourage ULTRASAT to try it out using the preliminary support for that mission that we have added. An M^{4}OPT command line option `--mission` which can take the values `uvex` or `ultrasat` selects all of the parameters described in Sections 3 and 4 (ETC model, bandpass, field of regard, FOV, slew speed, field grid, and so on) between those that are appropriate for UVEX or ULTRASAT respectively.

The M^{4}OPT model itself is not specific to space-based observations. With additional FOR and foreground models it could be extended to ground-based telescopes or even heterogeneous combinations of ground and space telescopes. In the future, we plan to extend it to ZTF, Vera Rubin Observatory, and other ground-based facilities. Ultimately, our vision is for M^{4}OPT to evolve into a scheduling toolkit featuring (1) a composable library of observing constraints inspired by the interface of the `astroplan` package (Morris et al. 2018), (2) uniform support for observers on the ground and in space, and (3) a globally optimizing scheduler.

When we constructed the luminosity function for the scheduler, we considered two KN models that are broadly consistent with GW170817 and plausible for BNS mergers: the jet-powered model of Piro & Kollmeier (2018) and the radioactively-powered model of Hotokezaka & Nakar (2020). However, the KN emission is likely to be qualitatively different and more varied for NS–BH mergers. Indeed, the masses and spins of the original compact objects, which we are able to measure with GW observations, can help us predict the nature of the remnant compact object and the KN emission (Margalit & Metzger 2019). If GW alerts included estimates of the masses, then we could use that information to taylor the times and depths of observations for the expected emission. Since the source lumninosity function in M^{4}OPT is configurable, in a future work we could evaluate mass-dependent observing strategies.

The scheduler currently considers a distribution of source absolute magnitudes, but not time variability of the source. This approach may be sufficient to optimize for obtaining a detection near peak, but is probably not sufficient to ensure a well-sampled light curve at later times. In a future work, we may add a light curve model which would allow the scheduler to automatically plan longer exposures before and after the predicted peak time of the KN emission.

Our probabilistic approach to scheduling and triggering follow-up observations can in principle allow for a more detailed treatment of the selection effects incurred during GW follow-up campaigns and astrophysical inference from the population of KNe observed by missions like UVEX. Developing a framework for KN inference with UVEX obser-

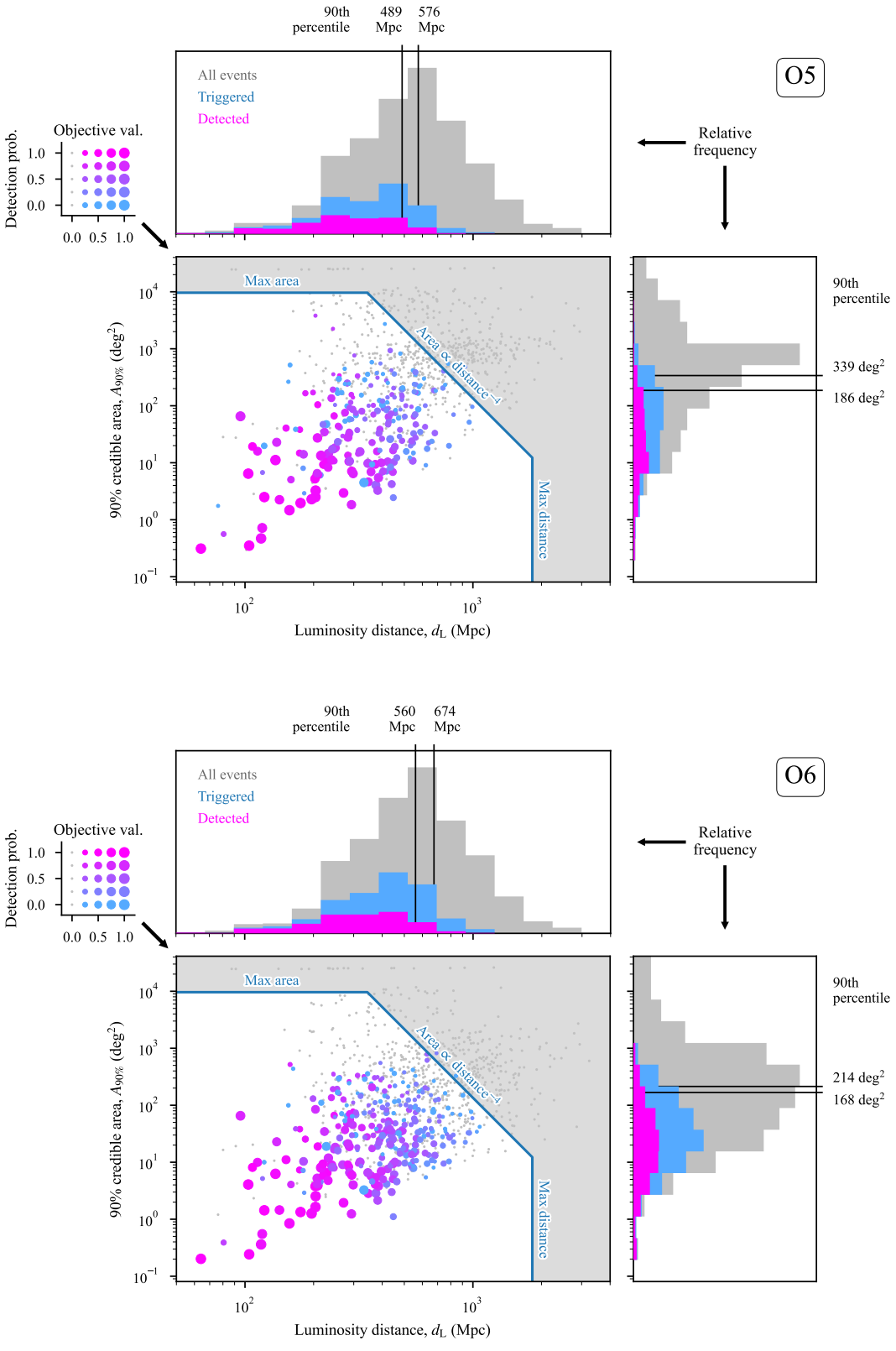

Figure 11. The distribution events selected for follow-up and detected for O5 and O6. Within each subfigure, there are three panels. **Bottom left panel:** scatter plot of 90% credible area versus distance. Events that were selected for follow-up with UVEX are represented by colored dots. The color of the dot represents the detection probability and the area of the dot represents the scheduler objective value. Events that were not selected for follow-up are marked with gray dots. The blue boundary represents the analytical predictor of the detection threshold given by Eqs. (2, 3, 4). **Upper panel:** distribution of luminosity distance, with 90th percentiles marked. **Right panel:** distribution of 90% credible area.

Table 4. Simulated events.

		Source frame masses		True position					
Run	Event ID	$m_1/M_\odot$	$m_2/M_\odot$	α/deg	δ/deg	$d_{\rm L}$/Mpc	$A_{90\%}$ / deg^2	Objective value[a]	Detection prob.[b]
O5	14	1.976	1.597	217.5627	+50.1543	204	3	0.95	0.92
O5	27	1.605	1.477	9.8234	+23.2808	685	571	<0.10	—
O5	30	1.318	1.280	337.1588	-36.0109	253	192	0.16	0.00
O5	41	1.979	1.772	194.5206	-19.3125	488	129	0.16	0.32
O5	46	6.405	2.379	139.4866	-25.4656	1277	766	<0.10	—
O5	52	6.754	2.218	335.1421	-3.1377	1457	90	<0.10	—
O5	54	1.961	1.583	131.7071	-38.2637	679	1143	<0.10	—
O5	60	25.417	2.561	91.4538	+78.0966	800	4579	<0.10	—
...	...	...	...	...	...	...	...	...	...

[a] The MILP solver is configured to stop early if it can prove that the objective value is less than 0.1.

[b] Events for which the objective value is less than 0.1 are not scheduled for follow-up, so they have a detection probability of zero.

NOTE—Table 4 is published in its entirety in a machine-readable format. A portion is shown here for guidance regarding its form and content.

Table 5. Expected number of events.

	O5	O6
Number of events selected	29^{+39}_{-18}	43^{+56}_{-26}
Number of events detected	12^{+18}_{-9}	17^{+24}_{-11}

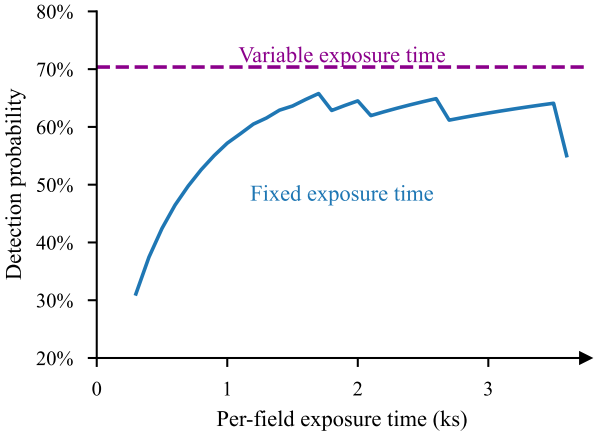

Figure 12. Detection probability versus exposure time for a single example event, resulting from the fixed exposure time strategy (see Section A.1). The horizontal dashed line shows the detection probability resulting from the variable exposure time strategy incorporating a distribution of absolute magnitudes (see Section A.3). The variable exposure time strategy is more likely to detect the counterpart than the fixed exposure time strategy, for any exposure time.

vations triggered by this method is an exciting direction of future work.

Some practical implementation details remain as future work to incorporate M^{4}OPT into the operations of a real observatory. For example:

- Our slew time constraints must conservatively model the dynamics of the actual spacecraft, including differing angular rates about different axes and keep-out constraints that must hold through the entire slew trajectory.
- We must be able to retrieve the spacecraft ephemeris from a live data source rather than evaluating it from a predefined orbital model.
- We must incorporate pre-defined segments of observing dead time for housekeeping events such as preplanned ground contacts and momentum dumping maneuvers.

Like the ZTF scheduler (Bellm et al. 2019) and the Vera Rubin Observatory scheduler (Naghib et al. 2019), we see M^{4}OPT as both a core component of the ground software system that enables fully autonomous observation planning and execution, and also an approachable and well-documented part of the guest observer science tools for a mission. Its permissive open-source licensing and open development model, free from the encumbrances of NOSA, are essential to those goals.

We hope to build from it a community tool that serves many missions from the concept phase all the way through operations. Also, integration of M^{4}OPT with community follow-up platforms such as the Gravitational Wave Treasure Map (Wyatt et al. 2020) could open possibilities for more effective and more meaningfully coordinated follow-up observations by multiple independently-operated facilities.

This work was performed in part at the Aspen Center for Physics, which is supported by the U.S. National Science Foundation (NSF) grant PHY-2210452.

This work used Expanse at the San Diego Supercomputing Center (SDSC) and Delta at the National Center for Supercomputing Applications (NCSA) through allocation AST200029, "Towards a complete catalog of variable sources to support efficient searches for compact binary mergers and their products," from the Advanced Cyberinfrastructure Coordination Ecosystem: Services & Support (ACCESS) program, which is supported by NSF grants #2138259, #2138286, #2138307, #2137603, and #2138296.

SCL and MWC acknowledge support from NSF with grant numbers PHY-2308862 and PHY-2117997.

We thank Steve Crawford at NASA Headquarters for help and support with the NASA software release process.

The code, data, and software environment to reproduce the figures and tables in this paper are available from Zenodo (Singer 2025).

This is LIGO document P2500008-v2.

Software: `astropy` (Astropy Collaboration et al. 2013, 2018), `astroquery` (Ginsburg et al. 2019), `dust_extinction` (Gordon 2024), `dustmaps` (Green 2018), `healpix` (Górski et al. 2005), `healpy` (Zonca et al. 2019), `ligo.skymap` (Singer & Price 2016; Singer et al. 2016a,b), `matplotlib` (Hunter 2007), `m4opt` (Singer et al. 2025), `numpy` (Harris et al. 2020), `regions` (Bradley et al. 2022), `scipy` (Virtanen et al. 2020), `spiceypy` (Annex et al. 2020), `sympy` (Meurer et al. 2017), `synphot` (STScI Development Team 2018)

APPENDIX

A. MILP PROBLEM DETAILS

In this appendix, we develop an MILP formulation of the problem of planning and scheduling GW ToO observations on a large FOV telescope. In Section A.1, we start with a simple but realistic problem in which we require multiple visits of each selected field that must all obey the FOR and slew speed limitations of the telescope. In Sections A.2 and A.3, we add progressively more detail, finally arriving at the full dynamic exposure time problem. All three formulations from Sections A.1, A.2, and A.3 are implemented in M^{4}OPT.

A.1. *Problem 1: Fixed Exposure Time*

We receive a HEALPix probability sky map that describes the probability distribution of the true but unknown position of a target of interest as a function of position on the sky. There is a delay between the time that the event occurred and when we can start observations due to the time it takes to uplink commands to the spacecraft, and there is a deadline by which we must complete our observations.

Our telescope can observe any of a set of n_J fields at predetermined sky locations in order to tile the sky map. For each field that we select, our telescope must visit the field at least n_K times. We have a cadence requirement that each visit of a given field must occur at least a time γ after the previous visit. Multiple visits with a minimum cadence are essential in short timescale transient searches to rule out moving solar system objects, which otherwise are a major contaminant.

Every visit takes a certain amount of exposure time, and it takes a known amount of time to slew between different fields. We may only a visit a field when it is within the FOR, the region that constrains where the telescope may point at any given instant of time.

A.1.1. *Data Preparation*

1. Construct a discrete 1D grid of times that stretch from the delayed start of observations up to the deadline.
2. Propagate the orbit of the spacecraft to calculate the position of the spacecraft at each time step.
3. For each field and each time step, test whether the field is within the instantaneous FOR, creating an observability bit map.
4. Transform the observability bit map into a list of time segments during which each field is observable.
5. Discard segments shorter than the exposure time.
6. Discard fields that have no observable segments.
7. For each field, find the HEALPix pixel indices that are within the field's footprint.
8. Select the 50 fields that contain the greatest probability, summed over the respective HEALPix pixels.
9. Discard pixels that are not contained in any field.
10. Calculate the slew times between all pairs of distinct fields.

A.1.2. *Problem Setup*

Index sets —

pixels	$I = \{0, 1, \ldots, n_I - 1\}$
fields	$J = \{0, 1, \ldots, n_J - 1\}$
visits	$K = \{0, 1, \ldots, n_K - 1\}$
observable segments	$(M_j = \{0, 1, \ldots, n_{Mj}\})_{j \in J}$
fields containing pixel i	$(J_i = \{0, 1, \ldots, n_{Ji}\})_{i \in I}$

Parameters —

probability of pixel i	$(\rho_i)_{i \in I}$
slew time from field j to j'	$(\sigma_{jj'})_{j \in J, j' \in J}$
start times of segments	$(\alpha_{jm})_{j \in J, m \in M}$
end times of segments	$(\omega_{jm})_{j \in J, m \in M}$
exposure time	ϵ
cadence, time between visits	γ
delay	β
deadline	δ

Binary decision variables —

pixel i is in any selected field	$(p_i)_{i \in I}$
field j is selected	$(r_j)_{j \in J}$
field j visit k is in segment m	$(s_{jkm})_{j \in J, k \in K, m \in M \mid n_{Mj} > 1}$

Continuous decision variables —

mid time of field j visit k	$(t_{jk})_{j \in J, k \in K}$

A.1.3. *Constraints*

Containment —Only count pixels that are in one or more selected fields.

$$\forall i: \quad p_i \leq \sum_{j \in J_i} r_j \tag{A1}$$

Cadence —If a field is selected for observation, then enforce a minimum time between visits.

$$\forall k > 1,\ j: \quad t_{jk} - t_{j,k-1} \geq (\epsilon + \gamma) r_j \tag{A2}$$

No overlap —Observations cannot overlap in time; they must be separated by at least the exposure time plus the slew time.

$$\forall j' > j,\ k,\ k' : \\ |t_{jk} - t_{j'k'}| \geq (\sigma_{jj'} + \epsilon)\,(r_j + r_{j'} - 1) \quad \text{(A3)}$$

FOR —An observation of a field can only occur while the coordinates of the field are within the FOR. For fields that have one observable segment ($n_{Mj} = 1$), this constraint is simply an inequality:

$$\forall j,\ k\ , m \mid n_{Mj} = 1 : \quad \alpha_{jm} + \epsilon/2 \leq t_{jk} \leq \omega_{jm} - \epsilon/2 \quad \text{(A4)}$$

For fields that have more than one observable segment ($n_{Mj} > 1$), we use the decision variable s_{jkm} to determine which inequality is satisfied:

$$\forall j,\ k\ , m \mid n_{Mj} > 1 : \\ s_{jkm} = 1 \ \Rightarrow\ \alpha_{jm} + \epsilon/2 \leq t_{jk} \leq \omega_{jm} - \epsilon/2 \quad \text{(A5)}$$

$$\sum_m s_{jkm} \geq 1 \quad \text{(A6)}$$

A.1.4. *Cuts*

Total exposure time —Although it is implied by other constraints, the constraint that the total exposure time cannot exceed the total available time is found to speed up the search. We add it as a cut: an inequality that the MILP may use to help guide its search but that is not checked when evaluating integer feasibility.

$$\sum_{j \in J} r_j \leq \frac{\delta - \beta}{\epsilon n_K} \quad \text{(A7)}$$

A.1.5. *Objective*

Maximize the sum of the probability of all of the pixels that are contained within selected fields:

$$\sum_{i \in I} \rho_i p_i \quad \text{(A8)}$$

A.2. *Problem 2: Variable Exposure Time*

In this variation, we have a sky map of the exposure time required to detect the source as a function of its position on the sky. We permit the exposure time to vary for each field. A given pixel counts toward the objective value only if the exposure time of a field that contains that pixel exceeds the pixel's exposure time.

A.2.1. *Problem Setup*

Additional parameters —

min exposure time to detect a source in pixel i	$(\epsilon_i)_{i \in I}$
min allowed exposure time	$\epsilon_{\min}$
max allowed exposure time	$\epsilon_{\max}$

Additional, semicontinuous decision variables —

exposure time of field j

$$(e_j)_{j \in J}, \forall j \in J : e_j = 0 \text{ or } \epsilon_{\min} \leq e_j \leq \epsilon_{\max}$$

A.2.2. *Constraints*

The constraints are slightly different.

Depth —Only count pixels that are observed to sufficient exposure time.

$$\forall i \in I : \quad p_{\rm i} = 1 \Rightarrow \max_{j \in J_i} e_j \geq \epsilon_i \quad \text{(A9)}$$

Exposure time —If a field's exposure time is nonzero, then it is selected for observation.

$$\forall j \in J : \quad \epsilon_{\max} r_j \geq e_{\rm j} \quad \text{(A10)}$$

Cadence —This is similar to Eq. (A2), except that we replace the right-hand side of the inequality.

$$\forall k > 1,\ j : \quad t_{jk} - t_{j,k-1} \geq \gamma r_j + e_j \quad \text{(A11)}$$

No overlap —This is also similar to Eq. (A3), except with a slightly different right-hand side.

$$\forall j' > j,\ k,\ k' : \\ |t_{jk} - t_{j'k'}| \geq \sigma_{jj'}\,(r_j + r_{j'} - 1) + (e_j + e_{j'})/2 \quad \text{(A12)}$$

FOR —This is similar to Eqs. (A4, A5), except that we replace ϵ with e_j. For fields that have one observable segment:

$$\forall j,\ k\ , m \mid n_{Mj} = 1 : \\ \alpha_{jm} + e_j/2 \leq t_{jk} \leq \omega_{jm} - e_j/2 \quad \text{(A13)}$$

For fields that have more than one observable segment:

$$\forall j,\ k\ , m \mid n_{Mj} > 1 : \\ s_{jkm} = 1 \ \Rightarrow\ \alpha_{jm} + e_j/2 \leq t_{jk} \leq \omega_{jm} - e_j/2 \quad \text{(A14)}$$

$$\sum_m s_{jkm} \geq 1 \quad \text{(A15)}$$

A.2.3. *Cuts*

Total exposure time —Replace Eq. (A7) with:

$$\sum_{j \in J} r_j \leq \frac{\delta - \beta}{\epsilon_{\min} n_K} \quad \text{(A16)}$$

$$\sum_{j \in J} e_j \leq \frac{\delta - \beta}{n_K} \quad \text{(A17)}$$

A.2.4. *Objective*

Same as in Section A.1.5 above.

A.3. *Problem 3: Variable Exposure Time with Prior Distribution of Absolute Magnitude*

In this variation, we don't know the precise absolute magnitude X of the source. In the case of KNe, our prior knowledge about the absolute magnitude is scant; for the sake of mathematical convenience, we assume that the absolute magnitude has a normal distribution, $X \sim \mathcal{N}[\mu_X, \sigma_X]$. We need to compute the distribution of *apparent* magnitudes x in order to determine the probability of detection as a function of exposure time for each pixel.

Gravitational-wave sky maps provide the posterior distribution of distance, as a parametric ansatz distribution (Singer et al. 2016a,b),

$$p(r) = \frac{N}{\sqrt{2\pi}\sigma} \exp\left[-\frac{1}{2}\left(\frac{r-\mu}{\sigma}\right)^2\right] r^2,$$

with the location parameter μ, scale parameter σ, and normalization N tabulated for each pixel. This is an inconvenient distribution for integration, so instead we construct a log-normal distance distribution with the same mean and standard deviation as the ansatz distribution.

We calculate the mean m and standard deviation s from μ and σ using the function `parameters_to_moments` from `ligo.skymap`[6]. Then, the location and scale parameters of the log-normal distribution are given by

$$\mu_{\ln r} = \ln m - \frac{1}{2}\ln\left(1 + \frac{s^2}{m^2}\right) \tag{A18}$$

$${\sigma_{\ln r}}^2 = \ln\left(1 + \frac{s^2}{m^2}\right). \tag{A19}$$

The logarithm of the distance then has the distribution $\ln r \sim \mathcal{N}[\mu_{\ln r}, \sigma_{\ln r}]$. The apparent magnitude is related to the absolute magnitude through $x = X + 5\log_{10} r + 25$, assuming that r is in the units of Mpc. Therefore the apparent magnitude has the distribution $x \sim \mathcal{N}[\mu_x, \sigma_x]$, with

$$\mu_x = \mu_X + \left(\frac{5}{\ln 10}\right)\mu_{\ln r} + 25 \tag{A20}$$

$${\sigma_x}^2 = {\sigma_X}^2 + \left(\frac{5}{\ln 10}\right)^2 {\sigma_{\ln r}}^2. \tag{A21}$$

With this Gaussian distribution of apparent magnitudes, we can now calculate the detection efficiency for each pixel: the probability that we detect the source assuming that the source is in that pixel, as a function of exposure time. For the purpose of implementation of this function in a MILP, we approximate it with a piecewise linear function, as illustrated in Fig 13.

[6] https://lscsoft.docs.ligo.org/ligo.skymap/distance/

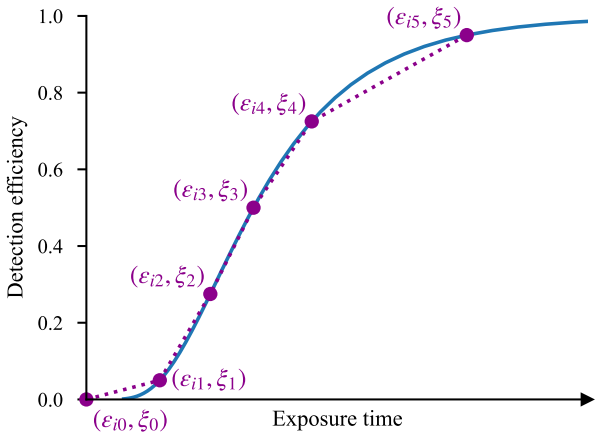

Figure 13. Piecewise linear approximation of the detection efficiency for a given pixel. In this example, we have assumed that the exposure time is inversely proportional to the square root of the flux, valid for sky background dominated imaging.

A.3.1. *Additional Data Preparation*

1. Use the function `parameters_to_moments` and Eqs. (A18, A20) to calculate the mean and standard deviation of the apparent magnitude in each pixel.

2. Select the desired quantiles for the piecewise linear approximation of the detection efficiency curve: for example, $(0, 0.05, 0.275, 0.5, 0.725, 0.95)$. For each pixel, calculate the exposure time required to achieve the specified detection efficiency.

A.3.2. *Problem Setup*

Additional index sets —

indices of quantiles	$N = \{0, 1, \ldots, n_N\}$

Additional parameters —

quantiles of detection efficiency	$(\xi_n)_{n\in N}$
exposure time of quantiles	$(\epsilon_{in})_{i\in I, n\in N}$
piecewise linear functions	$(f_i : \mathbb{R}_{\geq 0} \to [0,1])_{i\in I}$

Additional, continuous decision variables —

change from binary to continuous	$(p_i)_{i\in I}$

A.3.3. *Additional Constraints*

Depth—Replace Eq. A9 with:

$$\forall i \in I: \quad \max_{j \in J_i} e_j \geq f_i(p_{\mathrm{i}})$$

A.3.4. *Objective*

Same as in Section A.1.5 above.

REFERENCES

Aasi, J., Abadie, J., Abbott, B. P., et al. 2014, ApJS, 211, 7, doi: 10.1088/0067-0049/211/1/7

Abbott, B. P., Abbott, R., Abbott, T. D., et al. 2016, ApJL, 826, L13, doi: 10.3847/2041-8205/826/1/L13

—. 2017a, PhRvL, 119, 161101, doi: 10.1103/PhysRevLett.119.161101

—. 2017b, ApJL, 848, L12, doi: 10.3847/2041-8213/aa91c9

—. 2017c, Nature, 551, 85, doi: 10.1038/nature24471

—. 2017d, ApJL, 848, L13, doi: 10.3847/2041-8213/aa920c

Annex, A., Pearson, B., Seignovert, B., et al. 2020, JOSS, 5, 2050, doi: 10.21105/joss.02050

Arcavi, I. 2018, ApJL, 855, L23, doi: 10.3847/2041-8213/aab267

Astropy Collaboration, Robitaille, T. P., Tollerud, E. J., et al. 2013, A&A, 558, A33, doi: 10.1051/0004-6361/201322068

Astropy Collaboration, Price-Whelan, A. M., Sipőcz, B. M., et al. 2018, AJ, 156, 123, doi: 10.3847/1538-3881/aabc4f

Bellm, E. C., Kulkarni, S. R., Barlow, T., et al. 2019, PASP, 131, 068003, doi: 10.1088/1538-3873/ab0c2a

Bilimoria, K. D., & Wie, B. 1993, Journal of Guidance Control Dynamics, 16, 446, doi: 10.2514/3.21030

Bradley, L., Deil, C., Patra, S., et al. 2022, astropy/regions: v0.6, v0.6, Zenodo, doi: 10.5281/zenodo.6374572

Cenko, S. B. 2019, in American Astronomical Society Meeting Abstracts, Vol. 234, American Astronomical Society Meeting Abstracts #234, 212.03

Chan, M. L., Hu, Y.-M., Messenger, C., Hendry, M., & Heng, I. S. 2017, ApJ, 834, 84, doi: 10.3847/1538-4357/834/1/84

Chen, D.-S., Batson, R. G., & Dang, Y. 2009a, Applied Integer Programming (John Wiley & Sons, Ltd), doi: 10.1002/9781118166000

—. 2009b, Transformation Using 0–1 Variables (John Wiley & Sons, Ltd), 54–78, doi: 10.1002/9781118166000.ch3

Coughlin, M., & Stubbs, C. 2016, Experimental Astronomy, 42, 165, doi: 10.1007/s10686-016-9503-4

Coulter, D. A., Foley, R. J., Kilpatrick, C. D., et al. 2017, Science, 358, 1556, doi: 10.1126/science.aap9811

Criswell, A. W., Leggio, S. C., Coughlin, M. W., et al. 2025, arXiv e-prints, arXiv:2501.14109. https://arxiv.org/abs/2501.14109

Decleir, M., Gordon, K. D., Andrews, J. E., et al. 2022, ApJ, 930, 15, doi: 10.3847/1538-4357/ac5dbe

Dorsman, B., Raaijmakers, G., Cenko, S. B., et al. 2023, ApJ, 944, 126, doi: 10.3847/1538-4357/acaa9e

Drout, M. R., Piro, A. L., Shappee, B. J., et al. 2017, Science, 358, 1570, doi: 10.1126/science.aaq0049

Eichler, D., Livio, M., Piran, T., & Schramm, D. N. 1989, Nature, 340, 126, doi: 10.1038/340126a0

Fitzpatrick, E. L., Massa, D., Gordon, K. D., Bohlin, R., & Clayton, G. C. 2019, ApJ, 886, 108, doi: 10.3847/1538-4357/ab4c3a

Fong, W., & Berger, E. 2013, ApJ, 776, 18, doi: 10.1088/0004-637X/776/1/18

Free Software Foundation. 2006, Various Licenses and Comments about Them. https://www.gnu.org/licenses/license-list.html#NASA

Freiburghaus, C., Rosswog, S., & Thielemann, F. K. 1999, ApJL, 525, L121, doi: 10.1086/312343

Ginsburg, A., Sipőcz, B. M., Brasseur, C. E., et al. 2019, AJ, 157, 98, doi: 10.3847/1538-3881/aafc33

Goldstein, A., Veres, P., Burns, E., et al. 2017, ApJL, 848, L14, doi: 10.3847/2041-8213/aa8f41

Gordon, K. 2024, JOSS, 9, 7023, doi: 10.21105/joss.07023

Gordon, K. D., Cartledge, S., & Clayton, G. C. 2009, ApJ, 705, 1320, doi: 10.1088/0004-637X/705/2/1320

Gordon, K. D., Clayton, G. C., Decleir, M., et al. 2023, ApJ, 950, 86, doi: 10.3847/1538-4357/accb59

Gordon, K. D., Misselt, K. A., Bouwman, J., et al. 2021, ApJ, 916, 33, doi: 10.3847/1538-4357/ac00b7

Górski, K. M., Hivon, E., Banday, A. J., et al. 2005, ApJ, 622, 759, doi: 10.1086/427976

Gottlieb, O., Nakar, E., Piran, T., & Hotokezaka, K. 2018, MNRAS, 479, 588, doi: 10.1093/mnras/sty1462

Green, G. M. 2018, JOSS, 3, 695, doi: 10.21105/joss.00695

Handley, L. B., Petigura, E. A., & Mišić, V. V. 2024, AJ, 167, 33, doi: 10.3847/1538-3881/ad0dfb

Harris, C. R., Millman, K. J., van der Walt, S. J., et al. 2020, Nature, 585, 357, doi: 10.1038/s41586-020-2649-2

Herner, K., Annis, J., Brout, D., et al. 2020, A&C, 33, 100425, doi: 10.1016/j.ascom.2020.100425

Hotokezaka, K., & Nakar, E. 2020, ApJ, 891, 152, doi: 10.3847/1538-4357/ab6a98

Huangfu, Q., & Hall, J. J. 2018, Mathematical Programming Computation, 10, 119, doi: 10.1007/s12532-017-0130-5

Hunter, J. D. 2007, CSE, 9, 90, doi: 10.1109/MCSE.2007.55

Kasen, D., Badnell, N. R., & Barnes, J. 2013, ApJ, 774, 25, doi: 10.1088/0004-637X/774/1/25

Kasen, D., Metzger, B., Barnes, J., Quataert, E., & Ramirez-Ruiz, E. 2017, Nature, 551, 80, doi: 10.1038/nature24453

Kasliwal, M. M., Nakar, E., Singer, L. P., et al. 2017, Science, 358, 1559, doi: 10.1126/science.aap9455

Kiendrebeogo, R. W. 2025, Simulation of HLVK Configuration for O5 and O6 Observation Runs: Gravitational Wave Detection Rates, Skymaps, and Multimessenger Parameters (November 2024 edition), Zenodo, doi: 10.5281/zenodo.14585837

Kiendrebeogo, R. W., Farah, A. M., Foley, E. M., et al. 2023, ApJ, 958, 158, doi: 10.3847/1538-4357/acfcb1

Kilpatrick, C. D., Foley, R. J., Kasen, D., et al. 2017, Science, 358, 1583, doi: 10.1126/science.aaq0073

Koch, T., Achterberg, T., Andersen, E., et al. 2011, Mathematical Programming Computation, 3, 103, doi: 10.1007/s12532-011-0025-9

Kulkarni, S. R., Harrison, F. A., Grefenstette, B. W., et al. 2021, arXiv e-prints, arXiv:2111.15608, doi: 10.48550/arXiv.2111.15608

Lattimer, J. M., & Schramm, D. N. 1974, ApJL, 192, L145, doi: 10.1086/181612

Leinert, C., Bowyer, S., Haikala, L. K., et al. 1998, A&AS, 127, 1, doi: 10.1051/aas:1998105

Li, L.-X., & Paczyński, B. 1998, ApJL, 507, L59, doi: 10.1086/311680

Liu, M.-X., Tong, H., Hu, Y.-M., et al. 2021, Research in Astronomy and Astrophysics, 21, 308, doi: 10.1088/1674-4527/21/12/308

Margalit, B., & Metzger, B. D. 2019, ApJL, 880, L15, doi: 10.3847/2041-8213/ab2ae2

Metzger, B. D. 2020, Living Reviews in Relativity, 23, 1, doi: 10.1007/s41114-019-0024-0

Metzger, B. D., & Berger, E. 2012, ApJ, 746, 48, doi: 10.1088/0004-637X/746/1/48

Meurer, A., Smith, C. P., Paprocki, M., et al. 2017, PeerJ Computer Science, 3, e103, doi: 10.7717/peerj-cs.103

Mighell, K. J. 2005, MNRAS, 361, 861, doi: 10.1111/j.1365-2966.2005.09208.x

Morris, B. M., Tollerud, E., Sipőcz, B., et al. 2018, AJ, 155, 128, doi: 10.3847/1538-3881/aaa47e

Murthy, J. 2014, ApJS, 213, 32, doi: 10.1088/0067-0049/213/2/32

Naghib, E., Yoachim, P., Vanderbei, R. J., Connolly, A. J., & Jones, R. L. 2019, AJ, 157, 151, doi: 10.3847/1538-3881/aafece

NASA. 2022, NASA Software Engineering Requirements, Tech. Rep. NPR 7150.2D, NASA Office of the Chief Engineer. https://nodis3.gsfc.nasa.gov/displayDir.cfm?t=NPR&c=7150&s=2D

NASA Science Mission Directorate. 2022, SMD Policy Document SPD-41a. https://science.nasa.gov/spd-41

National Academies of Sciences, Engineering, and Medicine. 2018, Open Source Software Policy Options for NASA Earth and Space Sciences (Washington, DC: The National Academies Press), doi: 10.17226/25217

—. 2021, Pathways to Discovery in Astronomy and Astrophysics for the 2020s, doi: 10.17226/26141

Nicholl, M., Berger, E., Kasen, D., et al. 2017, ApJL, 848, L18, doi: 10.3847/2041-8213/aa9029

Parazin, B., Coughlin, M. W., Singer, L. P., Gupta, V., & Anand, S. 2022, ApJ, 935, 87, doi: 10.3847/1538-4357/ac7fa2

Petrov, P., Singer, L. P., Coughlin, M. W., et al. 2022, ApJ, 924, 54, doi: 10.3847/1538-4357/ac366d

Pian, E., D'Avanzo, P., Benetti, S., et al. 2017, Nature, 551, 67, doi: 10.1038/nature24298

Piro, A. L., & Kollmeier, J. A. 2018, ApJ, 855, 103, doi: 10.3847/1538-4357/aaaab3

Planck Collaboration, Aghanim, N., Ashdown, M., et al. 2016, A&A, 596, A109, doi: 10.1051/0004-6361/201629022

Rickman, E., & Brown, J. 2024, Space Telescope Imaging Spectrograph Instrument Handbook for Cycle 33, Hubble Space Telescope User Documentation, STIS Instrument Handbook, Version 24.0, (Baltimore: STScI)

Sagiv, I., Gal-Yam, A., Ofek, E. O., et al. 2014, AJ, 147, 79, doi: 10.1088/0004-6256/147/4/79

San, M. 2024, JOSS, 9, 6648, doi: 10.21105/joss.06648

San, M., Herman, D., Erikstad, G. B., Galloway, M., & Watts, D. 2022, A&A, 666, A107, doi: 10.1051/0004-6361/202244133

Saunders, E. S., Lampoudi, S., Lister, T. A., Norbury, M., & Walker, Z. 2014, in Society of Photo-Optical Instrumentation Engineers (SPIE) Conference Series, Vol. 9149, Observatory Operations: Strategies, Processes, and Systems V, ed. A. B. Peck, C. R. Benn, & R. L. Seaman, 91490E, doi: 10.1117/12.2056642

Savchenko, V., Ferrigno, C., Kuulkers, E., et al. 2017, ApJL, 848, L15, doi: 10.3847/2041-8213/aa8f94

Schutz, B. F. 1986, Nature, 323, 310, doi: 10.1038/323310a0

Shappee, B. J., Simon, J. D., Drout, M. R., et al. 2017, Science, 358, 1574, doi: 10.1126/science.aaq0186

Shvartzvald, Y., Waxman, E., Gal-Yam, A., et al. 2024, ApJ, 964, 74, doi: 10.3847/1538-4357/ad2704

Singer, L. 2025, Data Release: Optimal Follow-Up of Gravitational- Wave Events with the UltraViolet EXplorer (UVEX), Zenodo, doi: 10.5281/zenodo.15176276

Singer, L., pre-commit ci[bot], dependabot[bot], et al. 2025, m4opt/m4opt, v1.0.0, Zenodo, doi: 10.5281/zenodo.15169912

Singer, L. P., & Price, L. R. 2016, PhRvD, 93, 024013, doi: 10.1103/PhysRevD.93.024013

Singer, L. P., Chen, H.-Y., Holz, D. E., et al. 2016a, ApJL, 829, L15, doi: 10.3847/2041-8205/829/1/L15

—. 2016b, ApJS, 226, 10, doi: 10.3847/0067-0049/226/1/10

Solar, M., Michelon, P., Avarias, J., & Garces, M. 2016, A&C, 15, 90, doi: 10.1016/j.ascom.2016.02.005

STScI Development Team. 2018, synphot: Synthetic photometry using Astropy, Astrophysics Source Code Library, record ascl:1811.001

Villar, V. A., Guillochon, J., Berger, E., et al. 2017, ApJL, 851, L21, doi: 10.3847/2041-8213/aa9c84

Virtanen, P., Gommers, R., Oliphant, T. E., et al. 2020, Nature Methods, 17, 261, doi: 10.1038/s41592-019-0686-2

Williams, H. 2013a, Model Building in Mathematical Programming (Wiley). https://learning.oreilly.com/library/view/model-building-in/9781118506172/

—. 2013b, Building integer programming models I (Wiley), 165–201. https://learning.oreilly.com/library/view/model-building-in/9781118506172/

Wyatt, S. D., Tohuvavohu, A., Arcavi, I., et al. 2020, ApJ, 894, 127, doi: 10.3847/1538-4357/ab855e

Zonca, A., Singer, L., Lenz, D., et al. 2019, JOSS, 4, 1298, doi: 10.21105/joss.01298